# A 94-GHz Extremely Thin Metasurface-Based BiCMOS On-Chip Antenna

Shiji Pan, *Student Member, IEEE*, Francis Caster, *Member, IEEE*, Payam Heydari, *Senior Member, IEEE*, and Filippo Capolino, *Senior Member, IEEE*

***Abstract*—A novel fully on-chip antenna based on a metasurface fabricated in a 180-nm BiCMOS process is presented. Inspired by the concept of high impedance surface (HIS), this metasurface is *not* used as a reflector below an antenna as commonly done. Instead, it is used as a radiator by itself. The extremely thin metasurface is composed of a patterned top two metal layers and the ground plane placed in the lowest metal layer in the process. The ground plane on the lowest metal layer of the process provides a solid shielding from the substrate and other possible circuitries. The fundamental of the antenna radiation and design are described. The measured antenna shows −2.5 dBi peak broadside gain with 8-GHz 3-dB gain bandwidth and an impedance bandwidth larger than 10 GHz. In its class of broadside radiating fully on-chip antennas, with a ground plane on the lower metal layer of the process, and without additional fabrication processing, this structure achieves the widest impedance bandwidth at W-band and one of the highest gain and gain bandwidth. It is noteworthy that this is achieved with an extremely thin antenna substrate thickness and a shielding ground plane.**

***Index Terms*—Artificial magnetic conductor, high-impedance surface, leaky wave antenna, Marchand balun, millimeter wave, millimeter wave antennas, on-chip antenna.**

## I. Introduction

THE aggressive transistor scaling and advances in fabrication process are the main driving forces of unprecedented growth in wireless technology in the last two decades. Traditionally, different modules of a wireless system are separately fabricated using different technologies to achieve the best system performance. For example, the baseband circuits are mostly realized in CMOS process while the power amplifiers are implemented in III-V compound semiconductor technologies. Moreover, planar antennas, used in personal wireless devices, are mostly fabricated on printed circuit board (PCB) type of substrate, e.g., Duroid and FR4. This type of integration thus involves multiple chip packaging and requires a relatively large area for the whole system. To alleviate this issue, system-in-package solutions have been examined to reduce the system form factor. However, the antenna, usually the largest component of the system, is still developed outside of the package.

Manuscript received January 09, 2014; revised April 13, 2014; accepted May 27, 2014. Date of publication June 12, 2014; date of current version September 01, 2014. This work was supported in part by Semiconductor Research Cooperation under Grant 2009-VJ-1962.

The authors are with the Department of Electrical Engineering and Computer Science, University of California, Irvine, Irvine, CA 92697-2625 USA (e-mail: shijip@uci.edu; fcasteri@uci.edu; payam@uci.edu; f.capolino@uci.edu).

Color versions of one or more of the figures in this paper are available online at http://ieeexplore.ieee.org.

Digital Object Identifier 10.1109/TAP.2014.2330575

At millimeter-wave (mm-wave) frequencies, when the antenna's form factor is in the order of several millimeters, new integration techniques including antenna in package (AIP) and on-chip antenna (OCA) are becoming feasible. In [1], a 60-GHz folded dipole antenna built on fused silica substrate was integrated together with a transmitter chipset inside a package. A short interconnection between the chipset and the antenna feed line was realized by flipping the antenna substrate such that the feed line touches the bond pad on the die directly. Antennas designed on package substrates usually show good radiation performance in terms of radiation efficiency and gain. In [2], an 11.5-dBi broadside gain was achieved from a $2 \times 2$ small patch array utilizing wirebond as the interconnection between the die and the feed line of the off-chip antenna. Although chip-to-chip interconnections (e.g., wirebond) show low insertion loss at mm-wave frequencies below 100 GHz their performance still suffers from fabrication tolerance including misalignment and deviations from desired length and shapes [3], which could be a detrimental factor at sub-mm-wave frequencies. In addition, the assembly requires specialized processes which would increase the cost.

Meanwhile, aided by advances in silicon technologies, the OCA has triggered a considerable interest, as it allows the ultimate on-die integration of the entire wireless transceiver, eliminating the need for any off-chip interconnection. Despite lower gain and efficiency compared to antennas in package, which has been recognized as having more potentials for 60-GHz application [1], OCAs offer the much smaller feed line interconnection losses, which could be a substantial advantage for higher frequencies, including sub-mm-wave systems. However, designing a high gain and high efficiency OCA is very challenging for several reasons [4]: i) because of the high permittivity and low resistivity of the silicon or SiGe substrate, an on-chip antenna with silicon substrate will lose much of its power inside the substrate, thereby resulting in low radiation efficiency and low gain; ii) more importantly, although a very wide input bandwidth could be achieved, because of its high permittivity, using silicon as substrate makes the antenna gain and radiation pattern susceptible to the size of the substrate as in [5]. Possible electromagnetic interference might also occur due to the coupling from the adjacent passives. This is due to the surface wave(s) excited inside the silicon substrate and the reflections that occur at the die edges. For an array of OCAs such as in [6], nonuniform radiation patterns from array elements could degrade the beam scanning accuracy and may even tilt the main beam direction.

Therefore, for a robust OCA design, a metallic layer to shield the antenna from the silicon substrate is desired. This can be

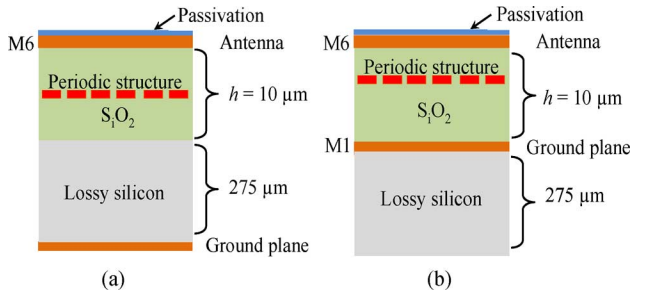


Fig. 1. Two different stack-up schemes to use an AMC in CMOS process: (a) the ground plane is below silicon and the wave penetrates the substrate; (b) extremely thin (10 $\mu$m) AMC with the ground plane on the lowest metal layer (M1) providing shielding from the silicon substrate. In this paper we provide a novel design that does not have the antenna over the AMC.

achieved by placing a ground plane at the lowest metal layer M1, such that the extremely thin silicon dioxide layer acts as the antenna substrate. However, because of the extremely thin thickness of silicon dioxide (i.e., less than 1% of the wavelength in silicon dioxide), the antenna bandwidth is, in general, very narrow. In [7], an elliptical slot antenna with a ground plane at M1 shows a 3.9% impedance bandwidth around 94 GHz. In [8], a slot antenna at top metal layer backed with a cavity using M1 shows a 6 GHz (4.3%) bandwidth at 140 GHz according to full wave simulations.

Recently, artificial magnetic conductor (AMC) or high-impedance surface (HIS) types of metasurface have been utilized for the OCA design [9]–[11]. Realized in the interlayers of the metal stack-up in silicon, these periodic structures act as reflection planes below the antenna to improve the antenna bandwidth and gain. The ground plane of these metasurfaces is placed *below* the lossy silicon, as shown in Fig. 1(a), to ensure the typical zero-degree phase crossing property typical of AMCs [12]–[14]. However, if the ground plane is placed on the bottom metal layer, i.e., M1, while the periodic structure is placed in the metal interlayers between top and bottom layer as shown in Fig. 1(b), the zero-phase crossing will not mostly occur and the metasurface will not exhibit high-impedance property. This detrimental effect is mostly due to excessive ohmic losses in the metasurface, as explained in [12], when the metasurface substrate becomes extremely thin as in this case when the ground is on M1. Therefore, it is very challenging to realize an AMC on the top metal layer of a silicon process with the ground plane at M1.

When the ground plane of metasurface is below the silicon substrate, as in Fig. 1(a), the OCA performance suffers from the excitation of surface wave(s) in the silicon substrate, leading to impairments such as losses, coupling, and higher sensitivity of antenna performance on the die's dimensions). It is worth mentioning that planar electromagnetic bandgap (EBG) structures, such as the mushroom geometry [13], can provide a stop-band for surface waves propagating inside the substrate. However, bandgap structures typically require the periodic structure to be connected to the ground plane with vias, to interact with the vertical electric field of the TM surface waves [13]. In the recent years, the through-silicon-vias (TSVs) has become available in customized CMOS technologies, and could meet the demand discussed above. However, in most standard processes, TSVs are still not available. Furthermore, at mm-wave frequencies the silicon substrate is rather thick in terms of the wavelength and hence full stop bands are rather difficult to be realized without additional die back-grinding.

In this paper, instead of using the metasurface as a high-impedance reflection surface below a radiating antenna, the metasurface is directly used as a radiator, without any dipole above it. It is important to note that the antenna ground plane in our design is placed on M1 to completely shield the wave propagating into the lossy silicon. Although the antenna is built on a very thin silicon dioxide substrate (i.e., a total thickness of 10 $\mu$m, around 0.6% of the wavelength inside $S_iO_2$), an 8-GHz 3-dB gain-bandwidth and an input bandwidth larger than 10 GHz has been achieved at 94 GHz with a proper feeding and matching network. This is, to the best of our knowledge, the largest impedance bandwidth achieved for a single-feed W-band (Bi)CMOS on-chip antenna built inside a silicon chip when there is a full antenna ground plane on M1. This work demonstrates the thinnest metasurface-inspired antenna with a thickness less than one percent of the wavelength.

This paper starts with a brief discussion on the possibility of realizing an on-chip HIS using two different metasurface configurations in Fig. 1. Next, in Section III, the design of the novel fully on-chip metasurface antenna (without a dipole above it) is detailed including the description of the leaky mode inside the metasurface, which has been proven as the radiation mechanism of this antenna. Section IV presents the design of an on-chip miniature size balun used to feed the proposed antenna. Section V presents the experimental results including the input reflection, broadside gain, radiation patterns for the metasurface antenna, and the s-parameters for the balun.

## II. On-Chip Metasurface as a Reflector

In [14], the metasurface composed of the dogbone shape elements was placed below a folded dipole antenna as an AMC to boost the antenna gain by 7 dB compared to a perfect electric conductor (PEC) ground, at 5.5 GHz. According to [15], this type of dogbone shape metasurface shows a couple of design advantages over other type of metasurfaces: i) it is fully planar and no via is required and ii) the resonant frequency is easily estimated by an electro- and magnetic static model simply from its geometrical parameters as long as the metasurface substrate is thin enough such that the fringing field effect and the coupling between adjacent dogbones could be neglected. The geometric parameters of single dogbone element used in this paper are shown in Fig. 2.

In [10], the metasurface made by dogbone shape elements was employed in an on-chip dipole-antenna design in a BiCMOS technology to enhance the antenna radiation at 94 GHz, assuming a ground plane *below* the silicon, as in Fig. 1(a). In Fig. 3, we show the cross-sectional view of the BiCMOS process with six metal layers and with a 275 $\mu$m thick, low resistivity silicon substrate. The unused metal layers will be filled with silicon dioxide. The simulated magnitude and phase of the plane wave reflection coefficient ($S_{11}$) of a metasurface made up of a dogbone using HFSS, a full wave finite element method (FEM) based simulation tool, are shown in Fig. 4(a). The simulation is conducted for normal incidence

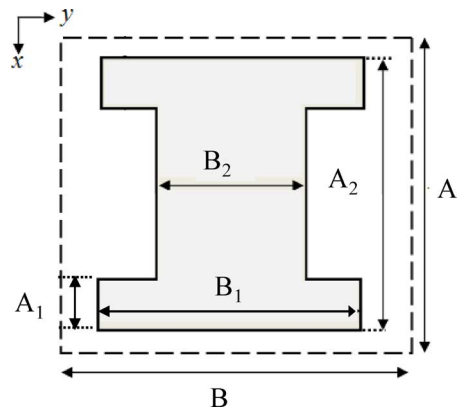


Fig. 2. Metasurface unit cell: geometry of a dogbone shape element for a high-impedance surface design.

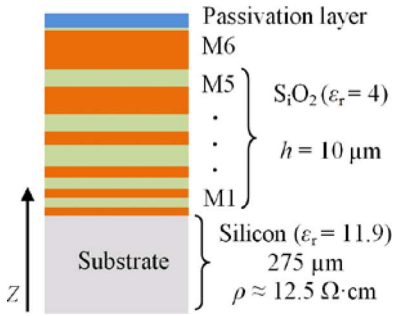


Fig. 3. Cross section (lateral) view of CMOS chip environment with six metal layers over the silicon substrate.

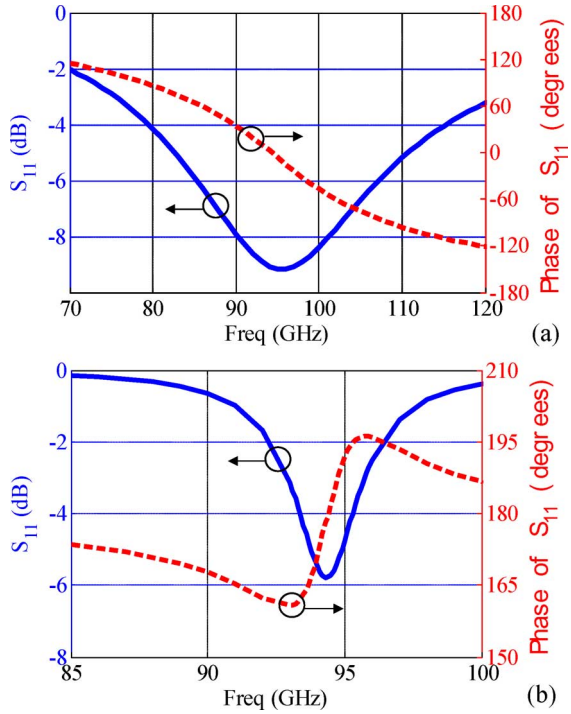


Fig. 4. Phase and amplitude of reflection coefficient of plane wave normal incidence, with electric field polarized along $x$, over a metasurface made of dogbones. (a) Configuration as in Fig. 1(a), where *the ground plane is below silicon* and the dimensions of the unit dogbone cell are $A = 0.4$, $B = 0.25$, $A_1 = 0.05$, $B_1 = 0.15$, $A_2 = 0.15$, and $B_2 = 0.09$ (all in mm). (b) The *extremely thin configuration* as in Fig. 1(b), where the *ground plane is on M1* with the dimension of unit cell as $A = 0.43$, $B = 0.43$, $B_2 = 0.12$, $B_1 = 0.42$, $A_1 = 0.12$, and $A_2 = 0.42$ (all in mm).

and electric field polarized along the main direction of the dogbone, i.e., the $x$-axis. It can be seen that at the resonance frequency (approximately 94 GHz), the zero-phase crossing occurs while the magnitude of $S_{11}$ reaches its minimum, around $-9$ dB. It is because at the resonant frequency, the current on the dogbone reaches the peak value as the ohmic losses reach its peak value. Similarly, in [9], an AMC made by a "snowflake" shape of periodic structures was shown to increase the gain of an on-chip loop antenna. However, both designs employ a ground plane below the silicon. Without an effective control of the surface waves inside the silicon substrate, several potential drawbacks may occur including strong electromagnetic interference (EMI) between OCA and other chip RF components [16], In addition, the antenna performance is vulnerable to the substrate dimension as demonstrated in [5].

Indeed, we have considered the configuration to place the ground plane on M1 (the lowest metal layer) and design the antenna and metasurfaces using the top five metal layers as shown in Fig. 1(b). Fig. 4 shows the magnitude and phase of the reflection coefficient of plane wave normal incidence over metasurface designed on the same BiCMOS process when the ground plane is on M1. The dogbone elements are placed on M5 while leaving top metal layer M6 free for possible location of a radiating antenna as shown in Fig. 1(b). Note that in this paper we use a metasurface with array of dogbones on M6 acting as a radiating antenna itself without any dipole on top. It can be observed that when the frequency increases, the phase of $S_{11}$ decreases but this trend is reversed at 93 GHz where the phase starts to grow. At the resonant frequency ($\sim$ 94 GHz), the reflection coefficient shows a phase of 180 degrees, which means the metasurface acts as an electric conductor rather than a magnetic conductor, since the latter requires a phase close to zero. In other words, the metasurface does not exhibit a high impedance. It is well known that placing a dipole very close to a PEC will result in a very low radiation efficiency due to the image dipole radiating with opposite phase [17]–[20]. In [12], a threshold condition for a metasurface to exhibit AMC properties was proposed. According to the discussion in [12], large ohmic losses make the AMC threshold condition fail, i.e., the metasurface cannot act as an HIS or as an AMC.

We conclude that when using the metasurface as a reflection plane, with a dipole located on its top, each configuration in Fig. 1 possesses some negative characteristics which may jeopardize its suitability in aiding OCA design in silicon. Despite this limitation in the next section we propose a novel idea for fully on-chip antennas based on metasurfaces, with the ground plane on M1, leading to an extremely thin antenna.

## III. High-Impedance Surface Antenna Without Dipole on Top

Instead of using the metasurface as reflection plane as traditionally done [17]–[20], it has been conceptually shown in [21] that the metasurface can be used as a radiator itself, without any dipole above it. That first conceptual idea was based on using a Duroid-type substrate and operating at microwave frequencies. The antenna thickness was around 4% of the free space wavelengths (around 6% of the wavelengths in the dielectric). In this paper, that concept is extended and further developed

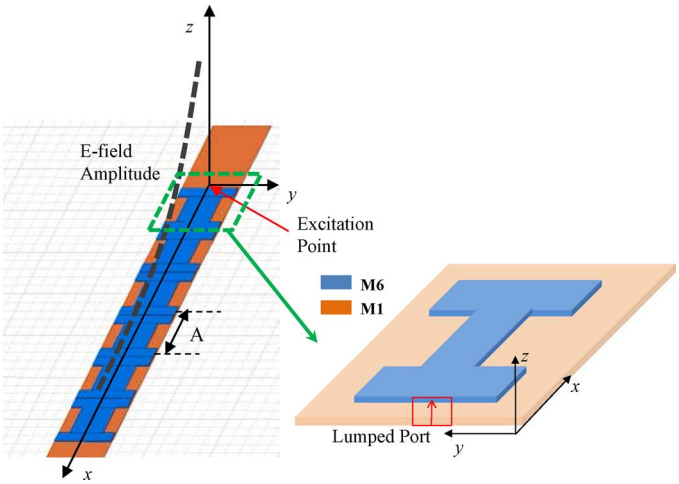


Fig. 5. Six dogbone elements aligned in the $x$-direction with the period A, and having periodic boundary along $y$, for high impedance surface design. The dashed line represents the exponential decay of a leaky wave excited at one edge.

to design and implement an on-chip antenna with its accompanying matching network at mm-wave frequencies, including fabrication and experimental results. Without a dipole on the top, the dogbones in the proposed metasurface-antenna design are placed on M6, the most top metal layer with the ground plane at the bottom layer (M1). Results will be further optimized using both M5 and M6 for the dogbones, as explained later in this paper. This results in an *extremely thin* thickness for the fully on-chip antenna equal to 0.27% of the free space wavelength and around 0.5% (i.e., 1/200) of the wavelength in the dielectric, making this possibly the thinnest metasurface antenna ever fabricated. This section starts by explaining the radiation mechanism and ways of improving the antenna performance. It will then go through the complete design of the metasurface antenna. Finally, the effects of the metasurface size on the antenna gain performance will be discussed.

### A. Mode Analysis

The in-plane modal analysis in [22] shows that a metasurface made by a periodic array of dogbone shaped conductors over a ground plane is able to support a TM "improper" leaky mode in the $x$-direction at a frequency range close to the magnetic resonance. Recall that an improper leaky wave decays along the $x$-direction and grows exponentially in the $z$ direction. This is usually the typical forward wave used in a leaky wave antenna [22], [23]. Indeed, the study in [22] was focused on the anti-symmetric mode supported by an array of paired and tightly coupled dogbone conductors, as in [15]. However, because of symmetry, those results are analogous to the case studied here: an array of dogbones over a conductor. In the following, we show that the radiation mechanism of the on-chip metasurface antenna is analyzed in terms of a TM leaky wave excited in the metasurface, propagating along the $x$-direction, as shown in Fig. 5. The full wave simulation is conducted using the finite-element-method provided by HFSS for six dogbone elements on M6 along the $x$-direction, assuming the periodic boundary condition along the $y$-direction. The dogbone element at the beginning of the row is excited by a lump port at its edge (as indicated in Fig. 5). The dimensions of the dogbones are as in the one used in Fig. 4(b), with the only difference that the dogbones are now placed on M6.

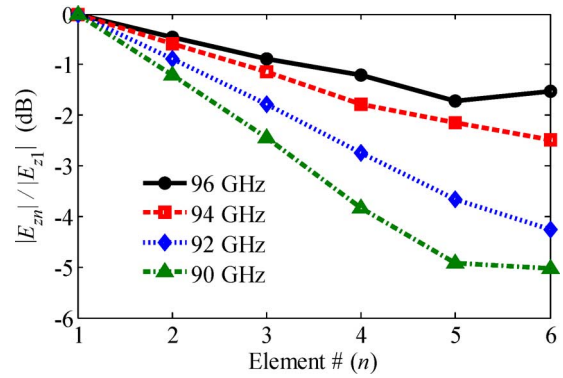


Fig. 6. Field magnitude versus element number (1~6) along the $x$-direction. Normalized with respect to the magnitude of the first sample.

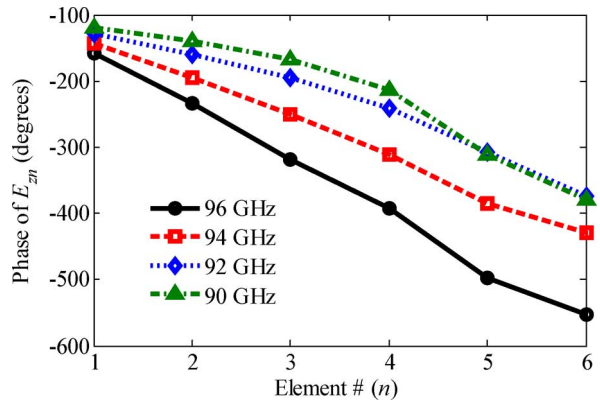


Fig. 7. Phase of field versus element number (1~6) along the $x$-direction.

The field over the "chain" of dogbones in Fig. 5, excited at one end, is sampled 2 $\mu$m below the central bar of each dogbone, once per unit cell in the $x$-direction with period A, at $x = (n-1) \times \mathrm{A} + 150$ $\mu$m, where $n$ is the element number (in this case, $\mathrm{A} = 430$ $\mu$m). The plot of the $z$-component of the electric field versus dogbone element number ($n$) is shown in Fig. 6. As it can be seen, for the four frequencies specified in Fig. 6 the field is decaying exponentially in the first several elements, as is typically the case for a leaky wave. As discussed in [21], the leaky mode is dominant in the first few dogbone elements close to the excitation, and away from it the so called "spatial field" term starts to play a major role, since the leaky wave itself becomes too weak. For more information about the excitation of leaky waves and spatial field terms in periodic structures, see [24]–[26]. Results in Fig. 6 show that the decay depends on the frequency. The phase variation of the field, evaluated at the same sample locations along the $x$-direction, is shown in Fig. 7, for a few frequencies close to the one of interest (94 GHz). The phase variation is more or less linear with the element number.

Therefore, as shown in Fig. 6 the field is highly dominated by a single leaky mode excited at the edge of the dogbone chain. Accordingly, every electric field component at the sampled points is expressed by

$$E(x = nd) = E_0\, e^{-j\beta_x nA} e^{-\alpha_x nA} \tag{1}$$

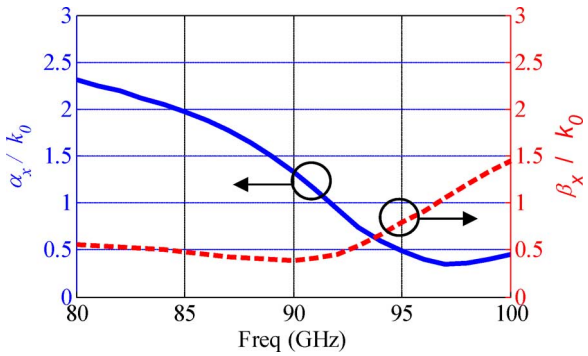


Fig. 8. Attenuation ($\alpha_x$) and phase constant ($\beta_x$) of the leaky wave along the $x$-direction, which is dominant in the first four dogbone elements. They are normalized with respect to the free space wave number.

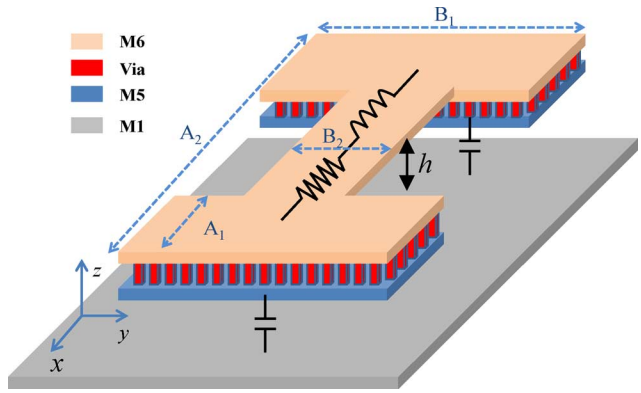


Fig. 9. Metasurface unit cell: a dogbone element comprised of metals on M6, M5, and the vias in between. The equivalent lump model is indicated. Extra capacitive effect occurs towards adjacent elements in the $x$-direction.

in which A is the period of the dogbones along $x$, $E_0$ is the field at the sample point closest to the excitation, and $\alpha_x$ and $\beta_x$ correspond to the attenuation and phase constants of the leaky mode. By curve-fitting for the first four dogbone elements from the excitation (i.e., $n = 1, \ldots, 4$), $\alpha_x$ and $\beta_x$ are retrieved. Their values, normalized by the free space wavenumber $k_0$, are plotted in Fig. 8. The phase constant of the leaky mode is smaller than that of the free space wavenumber below 97 GHz, implying that this mode is in the fast-wave region and hence radiating. The attenuation constant ($\alpha_x$) decreases as the frequency increases, whereas the phase constant ($\beta_x$) shows the opposite trend. At 94 GHz, $\beta_x \approx \alpha_x$, which has been indicated as the optimum condition for leaky wave radiation in the broadside direction [27]. Note that this is not a "standard" leaky wave antenna as the attenuation constant is not small, i.e., we are not exploiting leaky waves to create a large radiating aperture to form a highly directive antenna. Indeed, in a highly directive leaky wave antenna, the leaky mode would dominate the field on a very wide antenna aperture. Instead, here we expect that the spatial wave may also contribute to the total radiation [21], and the leaky mode is attenuating with $\alpha_x \approx 0.6k_0$, and therefore cannot cover a large aperture, though it is still radiating because $\beta_x < k_0$.

According to the full wave simulation, the phase of the reflection of a plane wave normally incident over the metasurface does not exhibit zero-phase crossing, similarly to what was shown in Fig. 4(b). However, the magnetic resonance still appears, associated with currents flowing in opposite directions on the dogbone and the ground plane [15], [28]. The absence of zero-phase reflection is attributed to ohmic losses as explained previously in [12].

It is known that close to the magnetic resonant frequency, there are strong ohmic losses on the dogbone due to the resonant current excited on the central part of dogbone and on the ground plane. Indeed, considering the dogbone over the ground plane, and assuming a current $I$ flowing on the central part (assumed a uniform current in the $x$ direction, for simplicity) connecting the two capacitors at the ends, the total ohmic loss in the dogbone conductor is $(1/2)I^2R_{\text{eff}}$ where the resistance of the dogbone is approximately given by $R_{\text{eff}} \approx \sigma_s(A_2 - A_1)/B_2$. An analogous resistance contribution associated with the current flowing over the ground plane should also be added. Therefore, to reduce the ohmic loss on the dogbone, a wider width of the dogbone central bar (i.e., a larger $B_2$) is desirable. However, a wider dogbone central bar implies also a smaller inductance according to the discussion in [15] since the inductance associated with a single dogbone's unit cell, comprising the dogbone and the ground plane, is given by $L_{\text{eff}} \approx \mu_0 h(A_2 - A_1)/B_2$. The magnetic resonant frequency is approximately estimated by $\omega \approx 1/\sqrt{L_{\text{eff}} \cdot C_{\text{eff}}}$, where $C_{\text{eff}}$ is the effective capacitor representing the two capacitance effects at the edges of the dogbone shown in Fig. 9. The effective capacitor is mainly contributed by i) the capacitance between the two dogbone arms and the ground plane, and ii) the capacitive coupling between two adjacent dogbones in the $x$-direction, when they are very close (gaps of the same order of $h$). A smaller resistance (by increasing $B_2$) implies a smaller inductance that will push the resonance to higher frequency. To compensate for this, in order to keep the same resonant frequency, the effective capacitor should be increased. For instance one could increase the size of the dogbone "arms" ($A_1B_1$). However, it would be preferable to keep a small size dogbone. Therefore, in this paper to increase the effective capacitance, we stack and combine two metal layers (M5 and M6) to form the dogbone arms such that the distance to the ground plane is smaller. In the layout, the dogbone arms at M5 and M6 are connected with array of 2 $\mu$m$\times$ 2 $\mu$m vias with the period of 4 $\mu$m in both $x$ and $y$ axis. Furthermore, to increase the $C_{\text{eff}}$, the dogbones are put close to each other in order to increase the capacitive coupling between the adjacent elements.

Within a total area limit, the design rule of the single dogbone element dimension is based on keeping the magnetic resonance around 94 GHz, while choosing $B_2$ as large as possible to decrease losses. The final optimized dimensions for the dogbones, which occupy both M5 and M6 as in Fig. 9, are $B_2 = 250$ $\mu$m, $B_1 = 420$ $\mu$m, $A_1 = 100$ $\mu$m, $A_2 = 500$ $\mu$m. A $= 506$ $\mu$m, and B $= 430$ $\mu$m.

### *B. Metasurface Antenna Design*

Fig. 10 shows the micrograph of the fabricated metasurface antenna made by a $3 \times 4$ array of dogbones with the unit cell dimensions provided at the end of Section III-A. As shown in Fig. 10, the two center rows of the dogbone are connected with metals bars to enhance antenna gain according to full wave simulations. A differential twin line is used to feed the antenna at the end of the two center rows of dogbone array.

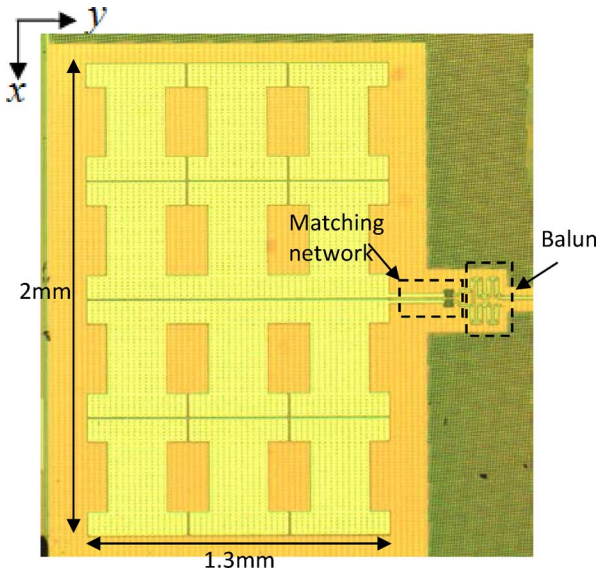


Fig. 10. Micrograph of the metasurface antenna including the matching network and the balun.

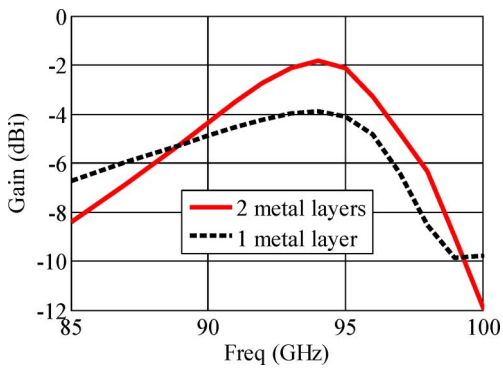


Fig. 11. Comparison of the broadside gain versus frequency of the metasurface antennas when the dogbone is using i) two metals layers (M5 and M6) and ii) single metal layer (M6 only).

Fig. 11 shows the simulated broadside gain for the proposed metasurface antenna made of a $3 \times 4$ array of dogbones. The dogbone array is fed by a differential mode from a waveguide port in the HFSS simulation. Two cases are considered: an array of dogbones on two metal layers (M5 and M6 as shown in Fig. 9), and the array of dogbone placed only on M6. When using array of dogbones on two metal layers, the dimension of the dogbones are the ones specified at the end of Section III-A. For the case of the metasurface realized only on a single metal layer (M6), the dimension of the dogbones are the ones used in Fig. 4(b). It is noteworthy that although the dogbones are placed on M5 for the results shown in Fig. 4(b), moving the dogbone with the same dimension from M5 to M6 does not change the resonant frequency, which is approximately independent of the metasurface thickness ($h$) as described in [15]. Comparing gain results for these two cases, it is observed that using two metal layers for each dogbone (M5 and M6 as in Fig. 9) improves the gain by 2 dB at the center frequency (94 GHz), as expected simply because the overall loss is lowered in this case.

For the purpose of the antenna measurement, a W-band balun is used to convert the single-ended signal associated with the W-band G-S-G probe to a balanced on-die differential signal. Also, an impedance matching network comprised of twin line and capacitors is designed between the metasurface antenna and balun (see Fig. 10).

TABLE I
SIMULATED PEAK GAINS AT 94 GHz FOR THE METASURFACE ANTENNA WITH DIFFERENT ARRAY SIZES

| Size | 4×3 | 4×2 | 6×2 | 6×3 |
|---|---|---|---|---|
| Directivity | 7.6 dB | 7.2 dB | 7.9 dB | 8.3 dB |
| Gain | - 1.8 dB | - 3 dB | - 2.78 dB | -1.5 dB |

The final geometry and the size of the dogbone array on M6, including the balun is shown in Fig. 10. The ground plane under the dogbone array on M1 at each edge is 100 $\mu$m and 150 $\mu$m larger than the dogbone array in $x$- and $y$-direction, respectively, making an area of 2.2 mm $\times$ 1.6 mm. Due to the extremely thin thickness of this metasurface, surface waves travelling along the silicon dioxide substrate carry very little power and therefore other dimensions of the finite size ground plane underneath the M6 dogbone layer would have little effect on the antenna gain. Indeed, according to the full wave simulations, as long as the length and width of the ground plane on M1 is 30 $\mu$m larger than that of the dogbone array on M6 (to collect all the fringe capacitance effects), there is literally no change in the antenna performance with increased size of the ground plane. This attribute is considered to be advantageous compared to other OCA design which uses ground plane below the silicon substrate, i.e., the OCA design in [5]. Furthermore, it is important to note that a full ground plane on M1 provides shielding to the silicon-based substrate under M1.

To satisfy the metal density rule, an array of 5 $\mu$m$\times$ 5 $\mu$m dummy fills are placed on all the metallic part of the antenna, on both the ground plane on M1 and the dogbones on M5 and M6. The dummy fills are also applied to other components mentioned in this paper, including the balun and microstrip line. It should be noted that due to the large memory requirements dummy holes and vias have not been included in the full wave simulations. For simulation purposes, the array of vias between M5 and M6 is replaced by bulk metal.

### C. Effect of Metasurface Array Size on Antenna Gain and Directivity

This section investigates the effect of the number of metasurface elements on the antenna gain. Simulations were conducted for metasurfaces with different numbers of array elements: $4 \times 3$ (the fabricated one), and $4 \times 2$, $6 \times 2$ and $6 \times 3$. For all these array sizes, the same twin line is used to feed the metasurface, and the ground plane on M1 is chosen as 100 $\mu$m larger than the dogbone array at each edge.

In Table I, the broadside directivity and gain for four different metasurface dimensions are compared. It is observed that the larger array size results in higher the antenna gain and directivity, although the amount of gain increase could be very small.

Fig. 12 shows the broadside gain versus frequencies for different array sizes. It is interesting to see that the peak of the broadside gain always occurs around 94 GHz, despite the array dimension, since the dogbone elements are kept identical in all

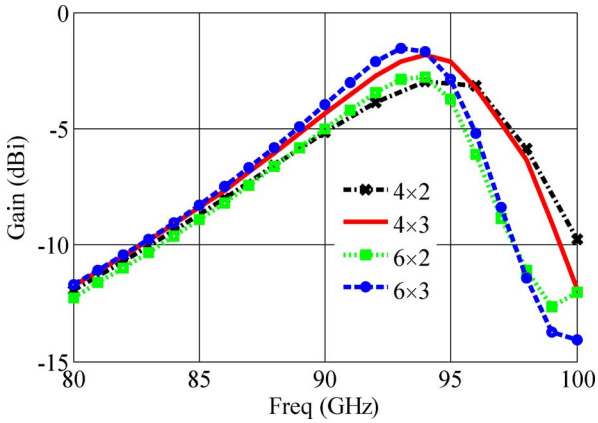


Fig. 12. Simulated broadside gain versus frequency for the proposed metasurface antenna with different element sizes.

cases. This is an important consideration in the design. Indeed, this is explained by noticing that the magnetic resonance frequency of the dogbone metasurface is very close to the leaky mode frequency in the metasurface as shown in [22]. Furthermore, one should note that the leaky mode is responsible for the antenna radiation, especially considering the optimum condition in Fig. 8 [27]. This represents simplicity in the design: the peak gain frequency of the proposed antenna could be estimated accurately by investigating the resonance frequency of a single element, which could be simply extracted by full wave simulations using periodic boundary conditions. It should also be noted that the radiation efficiency is low mainly due to the ohmic losses on the metals because of the *extremely thin* antenna substrate thickness.

An array size of $4 \times 3$ was chosen for the fabrication, which accounts for a tradeoff between the antenna gain and total area. It is noteworthy that decreasing the array size to $4 \times 2$, saving almost one-third of the die area compared to the $4 \times 3$ array, only lowers the antenna gain for 1 dB, which could also be considered in future designs. For an OCA design that is constrained to a smaller chip area, a smaller array size of $4 \times 2$ dogbones also provides a reasonable compromised solution.

## IV. Miniature-Sized Marchand Balun

As described in Section III-B, the proposed antenna requires differential feeding. To obtain a differential signal from a single-ended probe, a balun is to be designed. A Marchand balun [29] composed of two quarter wavelength couple lines is designed and developed for this design. The Marchand balun has been used for wide bandwidth designs at RF and microwave frequencies [30], [31]. In [32], the Marchand balun was also implemented in (Bi)CMOS technology at 60 GHz. Different techniques to miniaturize the dimension of the Marchand balun have been investigated in [31], [33], and [34].

Fig. 13 shows the top view of the Marchand balun designed using meander shaped couple line, referring the idea in [33]. The Meander-shape couple line replaces straight couple line and greatly shrinks the profile of the balun. Both the top half and bottom half of the couple lines are in the length of a quarter wavelength. The gap between the coupled lines is 2 $\mu$m. The mitered corners are used for bending the couple line while minimizing the insertion loss at the bends. The locations of the two

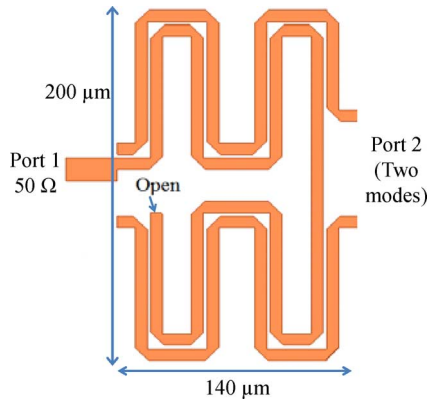


Fig. 13. Dimension of the Marchand balun.

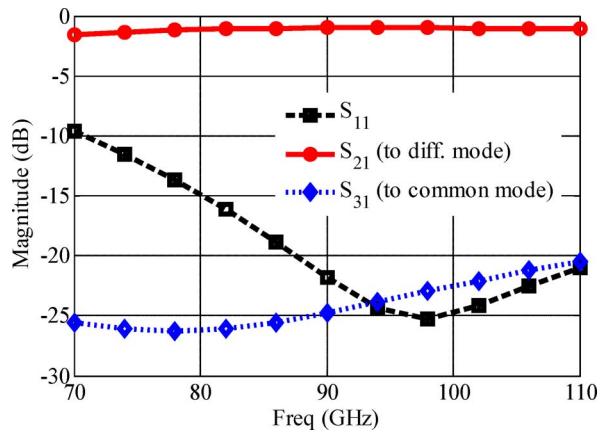


Fig. 14. Simulated input reflection and transmission to the differential mode and the common mode of the designed balun.

differential outputs are shifted a certain distance away from the center to achieve a near-perfect 180 degree out of phase difference between the two outputs. The total area of the balun is 140 $\mu$m$\times$ 200 $\mu$m.

Fig. 14 shows the simulated input reflection and transmission to two output modes, one differential mode and one common mode of the balun. It can be observed that the designed balun performs well in the whole W-band, from 70 GHz to 110 GHz, with below $-10$ dB input reflection, lower than $-20$ dB transmission to common mode output. The average insertion loss of the balun over W-band is around 1.5 dB. The balun is characterized experimentally in the next section.

## V. Measurement Results

### A. S-Parameters Characterization

For on-chip antenna measurement, one of the detrimental factors which will degrade the measurement accuracy is the possible electromagnetic interference (EMI) between the measuring probe and the antenna due to the proximity between them, as shown in [5]. To alleviate possible EMI for on-chip antenna measurement, a back-feeding scheme could be used for in-package antenna measurement as in [35] and [36]. However, due to the difficulty in having TSVs in commercial (Bi)CMOS processes, it is not straightforward to feed the OCA from the back-side of the radiating chip.

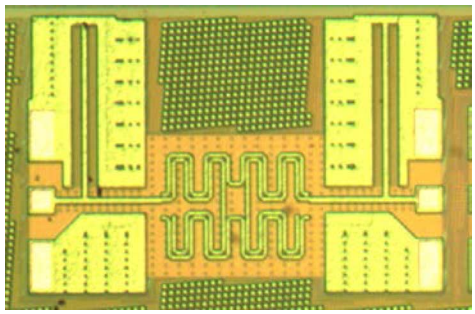

Fig. 15. Micrograph of two same baluns in back-to-back configuration.

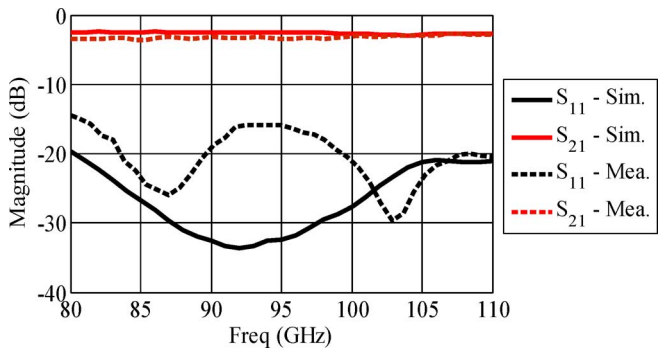


Fig. 16. Comparison of the simulated and the measured input reflection and transmission of the back-to-back baluns in Fig. 15.

To mitigate this issue, we consider separating the antenna and the measuring probe with a rather long on-chip feed line. In the present characterization, we have used a 2.5-mm-long microstrip line between the probe pad and the input of the balun. To accurately characterize the insertion loss, another 2.5-mm-long microstrip line is fabricated on the same die, and its measured and simulated results are shown in the Appendix, leading to an insertion loss of 3 dB.

To characterize the performance of the balun using single-ended probes, a back-to-back configuration made of two identical baluns is fabricated and the micrograph is shown in Fig. 15.

Fig. 16 shows the simulated and measured input reflection and transmission of the two back-to-back baluns. It can be observed that the measured results match well with the simulated ones, except for approximately 1 dB higher insertion loss. This result is consistent with the long microstrip line measurement shown in Appendix. Considering the symmetry, the measured insertion loss of a single balun is around 1.5 dB.

The differential input impedance of the metasurface before the feed twin line is shown in Fig. 17(a). Without any matching circuit, the metasurface shows a relatively flat input resistance and reactance in the frequency range between 90 GHz to 102 GHz, which implies a wide input bandwidth after proper matching. The matching circuit is shown in Fig. 17(b). The antenna matching network comprises a 230 $\mu$m long twin line ($Z_{0,diff} = 85\ \Omega$) and two finger capacitors (22 fF) in series with each line. When the matching network is connected in between the metasurface and the balun, the parameters of the matching network were optimized to achieve a largest possible impedance bandwidth at the input of the balun.

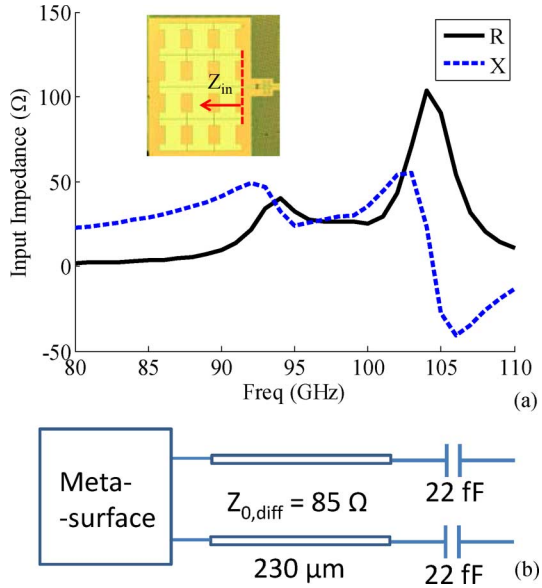


Fig. 17. (a) Input impedance of the metasurface observed at the feed edge of the metasurface itself as indicated in the figure with a dashed line. (b) Matching network between the metasurface and the balun.

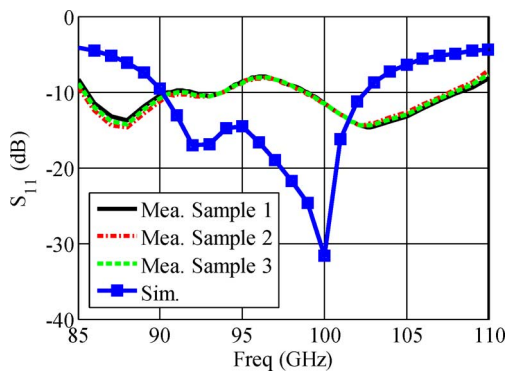


Fig. 18. Comparison of the simulated and the measured antenna input reflection coefficient at the input of the long 2.5-mm microstrip line.

The antenna input reflection is measured at the input of a 2.5-mm-long microstrip line. Fig. 18 shows the comparison between the simulated and measured antenna input reflection ($S_{11}$) from three separate antenna samples at the input of long microstrip line. The measured results for the three samples are consistent. The simulated $-10$ dB input bandwidth covers a wide frequency range between 90 and 102.5 GHz. The measured $S_{11}$ shows a certain discrepancy with the simulated one, especially in the frequency range between 95 to 110 GHz. This could be due to several reasons, including:

i) The full wave simulation does not include the dummy holes or the vias between M5 and M6. This affects the current flowing along the dogbone and the ground plane. If one considers the current flowing on the dogbone arms, because of the holes and the vias, the current flowing on the top surface of M6 could partially travel into the surfaces below, including the bottom surface of M6 and even the top and bottom surface of the M5. The metal layers M5, M6 and the vias in between shares similar thickness around 2 $\mu$m. Although the effect could be trivial in a

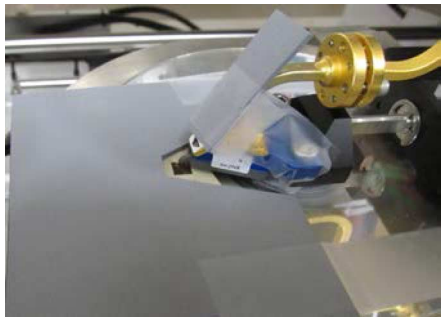

Fig. 19. Probed on-chip antenna with thin absorbers covering part of the probe-head, waveguide and wafer chuck.

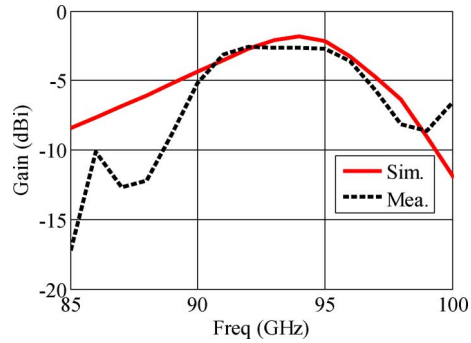


Fig. 20. Comparison of the measured and the simulated antenna broadside gain versus frequency.

short distance, the total effect could be summed up, and could thus play a strong effect since the antenna has a length ($x$-direction) longer than one $\lambda_g$ (the guided wavelength of microstrip line on silicon dioxide substrate).

ii) Possible variations in the thickness of metal layers and dielectric layers as stressed in [7]. Considering the thickness between M5 and the ground plane on M1 is less than 6 $\mu$m, a possible variation of $+/-0.5$ $\mu$m in any layer thickness would result in a relatively large deviation in the antenna substrate thickness.

iii) Variations in the material properties (dielectric permittivity and conductor conductivity) at mm-wave frequencies compared to microwave frequencies.

Nevertheless, since the measured $S_{11}$ between 90 and 102.5 GHz are all below or close to $-10$ dB, the deviation between simulation and measurement are reasonably small from the quantity point of view. To mitigate the deviation in the future work, it is desired to perform numerical simulations with fine details and have more accurate material electrical properties.

### *B. Antenna Gain and Radiation Pattern*

The same equipment setup and calibration scheme as described in [5] is used to measure the radiation property of the metasurface antenna. The OCA is measured in the receiving mode by receiving radiation from the transmitting W-band calibrated horn antenna which is fed by a frequency multiplier. The antenna gain is calculated as

$$G_{AUT} = P_{AUT} - P_{\text{horn}} + G_{\text{horn}} + Loss_p \qquad (2)$$

in which all the terms given are in dB scale: $P_{AUT}$ and $P_{\text{horn}}$ are the power received at the spectrum analyzer when using the antenna under test (AUT) and an additional calibrated horn as receiving antennas, respectively, with gain $G_{\text{horn}}$ (24 dBi at 94 GHz). Furthermore, $Loss_p$ is the total insertion loss including that from the probe (1 dB), the balun (1.5 dB), the 2.5-mm-long microstrip feed line (3 dB) and an estimated transition loss between probe tip and the on-chip CPW (0.5 dB), with a total loss of 6 dB. To suppress the reflection due to the presence of metallic objects close to the antenna, thin mm-wave absorbers are used to surround the antenna, and also to cover the wafer chuck and probe-head as shown in Fig. 19.

In Fig. 20, the measured broadside gain, indicated by dashed line, is obtained by averaging the measured data from three distinct gain measurements. The measured results show good correlation in the 3-dB gain bandwidth of the antenna with the full wave simulation. The peak gain is around $-2.5$ dBi in the frequency range between 92 to 95 GHz. The 3 dB gain bandwidth is around 8 GHz, from 89 GHz to 97 GHz. Considering the difficulties in measuring the fields on the metallic probe station and also considering the variety of calibration required for the measurement, the accuracy of the measurement is estimated as $\pm 1 \sim 1.5$ dB. Table II shows a comprehensive list of recent published work on single-feed mm-wave and Terahertz (THz) CMOS and BiCMOS fully on-chip antennas, radiating at the broadside direction, with a ground plane at the lower metal layer. Therefore for all these antennas, the substrate is extremely thin and the radiating zone is shielded from the lossy silicon substrate. Compared with other work, our proposed antenna shows the highest gain at W-band, and the widest relative impedance bandwidth achieved so far among all the shown designs at mm-wave and THz. It should be mentioned that when the frequency increases, and hence the substrate becomes electrically thicker, our proposed antenna has the potential to achieve even wider relative bandwidth and gain. Similarly, the improvement in terms of gain and bandwidth can be obtained also at W-band when considering other fabrication processes that allow substrate thickness larger than the one considered here (10 $\mu$m).

The normalized measured radiation patterns of the antenna at three different frequencies, including 94, 91.5 and 96.5 GHz in both E- and H-plane are shown in Fig. 20. Each measured pattern is compared against a simulated one. Due to the presence of certain obstacles in the probe station, the pattern measurement cannot be carried out in the complete E- and H-planes (see also [5]). In the H-plane, the measurement was done over only one quadrant and the range is limited by 40 degrees from the broadside direction. In the E-plane, the limit was 12 degrees in one quadrant and 50 degrees in the other quadrant. The pattern measurement was repeated twice in each plane and the curves shown are based on the averaging these two measured results. Measured patterns and simulated ones have similar trends. The ripple of the measured radiation pattern is possibly due to the interference between the probe and the AUT during measurement (see also [5]).

TABLE II
PERFORMANCE COMPARISON OF (Bi)CMOS BASED FULLY-ON-CHIP ANTENNAS OVER AN EXTREMELY-THIN SUBSTRATE WITH A GROUND PLANE AT THE LOWER METAL LAYER

| Reference | Process | Antenna type | Antenna substrate thickness (μm) | Freq. (GHz) | −10dB impedance BW (GHz) | Relative impedance BW (%) | Gain (dBi) | Size (mm×mm) |
|---|---|---|---|---|---|---|---|---|
| This work | 180 nm BiCMOS | Leaky wave | 10 | 94 | 10 | 10.6 % | −2.5 | 2 × 1.3 |
| [7] | 130 nm CMOS | Elliptical slot | 11 | 90 | 2.5 | 2.8 | − 6 | 1.7 × 1.1 |
| [8] | 180 nm BiCMOS | Slot | 10 | 140 | 5 | 3.6 | − 2 | 1.2 × 0.6 |
| [40] | 130 nm CMOS | Slot | NA | 9 | NA | NA | −10 | 0.5 × 0.5 |
| [41] | 130 nm CMOS | Patch | NA | 60 | 0.81 | 1.3% | −3.3 | 1.58 × 1.22 |
| [42] | 180 nm BiCMOS | Slot | 10 | 360 | NA | NA | −2.2 | 0.25 × 0.2 |
| [43] | 250 nm BiCMOS | Patch | 15 | 79 | 4 | 5% | −1.3 | 0.95 × 0.85 |
| [44] | 130 nm BiCMOS | SIW | NA | 410 | 12 | 2.9% | −0.5 | 0.5 × 0.2 |
| [45] | 45 nm CMOS | Patch | 4 | 410 | NA | NA | −1.5 | 0.2 × 0.2 |
| [46] | 65 nm CMOS | Patch | NA | 1000 | 24 | 2.4% | +1.5 | 0.068× 0.045 |
| [47] | 180 nm CMOS | Patch | < 10 | 60 | 1.5 | 2.5 | −14.5 | 1.15 × 1.15 |

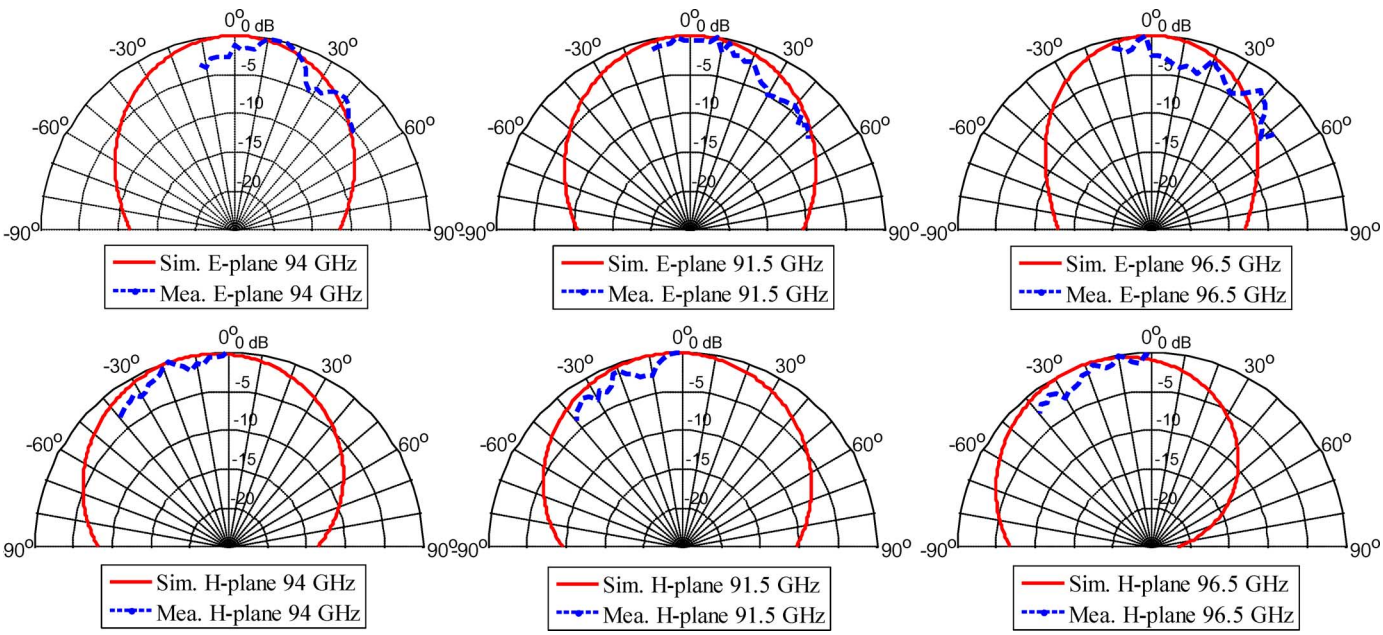


Fig. 21. Measured and simulated antenna radiation patterns in both the E- and H-planes at 94, 91.5, and 96.5 GHz.

## VI. CONCLUSION

It is known that for silicon based on-chip antenna designs, the presence of ground plane on the bottom metal layer (M1) usually causes low efficiency and very narrow bandwidth. Despite that, we have proposed the design of a fully on-chip antenna with a full ground plane on the bottom metal layer, inspired by previous studies on high impedance surfaces, that exhibits the great performance in terms of gain-bandwidth product at W-band for this class of antennas radiating at broadside. The presence of the metal ground plane on M1 is important to prevent leakage into the substrate and render the antenna performance independent of the die size because of its shielding. Having an on-chip antenna radiating at broadside, as in this paper, without the ground on M1 results in unstable radiation performance. This would occur even if the substrate is ground and a metal is placed underneath because of the strong coupling between antenna and the high permittivity substrate. It is also true that with off-chip components, placed above the chip, the antenna gain could be improved, even significantly. Examples include using lenses [37], placing dielectric resonators [38], [39], or superstrate [7] on top of the chip and feeding those with

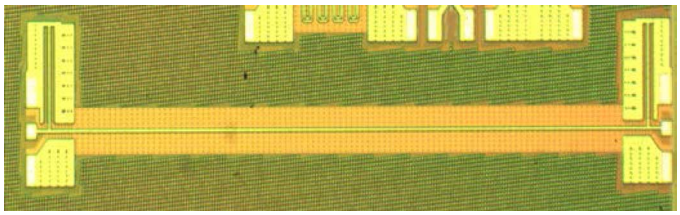

Fig. 22. Micrograph of a 2.5-mm-long 50 Ω microstrip line.

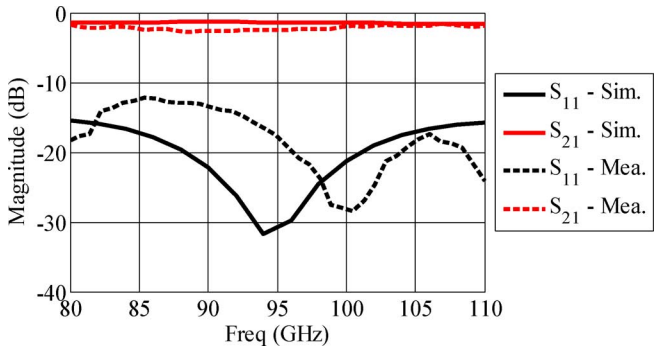


Fig. 23. Comparison of simulated and measured input reflection and transmission of the 2.5-mm microstrip line in Fig. 22. The long transmission line has been used to feed the antenna.

an on-chip launcher. Although the performance (efficiency and bandwidth) of these hybrid solutions are, in general, better than that of fully on-chip antennas, these techniques require additional processes, which may increase the cost and design complexity. On the contrary, the proposed fully on-chip antenna has been designed in a silicon process with no additional post-fabrication processing. At sub-mm-wave frequencies, it is expected that even better performance could be achieved by the proposed design due to the wavelength shrinkage.

## Appendix

Fig. 22 shows the micrograph of a 2.5-mm-long microstrip line with two ends connected to two bond pads. The bond pads are as those used in [5]. The parasitic capacitance of the bond pad is compensated with a shunt stub to achieve a stable impedance of 50 Ω at the input of the microstrip line over a wide frequency band (70–110 GHz).

The simulated, including the bond pads, and measured input reflection and transmission of the 2.5-mm-long microstrip line are compared in Fig. 23, providing a good agreement. For the insertion loss ($S_{21}$), there is an average 1 dB–1.8 dB deviation between the simulation and the measurement. The deviation stems from the fact that i) the electrical properties of the materials at mm-wave frequencies are a bit different from those provided by the foundry (used in the simulations) that are typically obtained below 10 GHz; and ii) possible wave leakage into silicon substrate and variation to metal conductivity could exist due to the existence of the dummy holes, thereby creating slightly higher losses in the long microstrip line.

## Acknowledgment

The authors would like to thank TowerJazz Semiconductor for antenna fabrication and ANSYS for providing us simulation tools. They would also like to thank Salvatore Campione, UC Irvine, for helping building the measurement setup.

## References

[1] U. R. Pfeiffer, J. Grzyb, L. Duixian, B. Gaucher, T. Beukema, B. A. Floyd, and S. K. Reynolds, "A chip-scale packaging technology for 60-GHz wireless chipsets," *IEEE Trans. Microw. Theory Tech.*, vol. 54, no. 8, pp. 3387–3397, Aug. 2006.

[2] S. Beer, H. Gulan, C. Rusch, and T. Zwick, "Coplanar 122-GHz antenna array with air cavity reflector for integration in plastic packages," *IEEE Antennas Wireless Propag. Lett.*, vol. 11, pp. 160–163, 2012.

[3] S. Beer, H. Gulan, M. Pauli, C. Rusch, G. Kunkel, and T. Zwick, "122-GHz chip-to-antenna wire bond interconnect with high repeatability," in *IEEE MTT-S Int. Microw. Symp. Dig. (MTT)*, 2012, pp. 1–3.

[4] Y. P. Zhang and D. X. Liu, "Antenna-on-chip and antenna-in-package solutions to highly integrated millimeter-wave devices for wireless communications," *IEEE Trans. Antennas Propag.*, vol. 57, no. 10, pp. 2830–2841, Oct. 2009.

[5] S. Pan, L. Gilreath, P. Heydari, and F. Capolino, "Investigation of a wideband BiCMOS fully on-chip W-band bowtie slot antenna," *IEEE Antennas Wireless Propag. Lett.*, vol. 12, pp. 706–709, 2013.

[6] F. Caster, L. Gilreath, S. Pan, Z. Wang, F. Capolino, and P. Heydari, "A 93-to-113 GHz BiCMOS 9-element imaging array receiver utilizing spatial-overlapping pixels with wideband phase and amplitude control," in *Proc. IEEE Int. Solid-State Circuits Conf. Dig. Tech. Papers (ISSCC)*, 2013, pp. 144–145.

[7] J. M. Edwards and G. M. Rebeiz, "High-efficiency elliptical slot antennas with quartz superstrates for silicon RFICs," *IEEE Trans. Antennas Propag.*, vol. 60, no. 11, pp. 5010–5020, Nov. 2012.

[8] S. Pan and F. Capolino, "Design of a CMOS on-chip slot antenna with extremely flat cavity at 140 GHz," *IEEE Antennas Wireless Propag. Lett.*, vol. 10, pp. 827–830, 2011.

[9] X. Y. Bao, Y. X. Guo, and Y. Z. Xiong, "60-GHz AMC-based circularly polarized on-chip antenna using standard 0.18-$\mu$m CMOS technology," *IEEE Trans. Antennas Propag.*, vol. 60, no. 5, pp. 2234–2241, May 2012.

[10] S. Pan, D. Wang, C. Guclu, and F. Capolino, "High impedance layer for CMOS on-chip antenna at millimeter waves," in *Proc. IEEE Int. Symp. Antennas Propag. (APSURSI)*, 2011, pp. 903–906.

[11] H. C. Kuo, H. L. Yue, Y. W. Ou, C. C. Lin, and H. R. Chuang, "A 60-GHz CMOS sub-harmonic RF receiver with integrated on-chip artificial-magnetic-conductor Yagi antenna and balun bandpass filter for very-short-range gigabit communications," *IEEE Trans. Microw. Theory Tech.*, vol. 61, no. 4, pp. 1681–1691, Apr. 2013.

[12] S. Pan, C. Guclu, and F. Capolino, "Effect of losses on the performance of very thin artificial magnetic conductors," in *Proc. URSI Int. Symp. Electromagn. Theory (EMTS)*, 2013, pp. 404–407.

[13] D. Sievenpiper, L. Zhang, R. F. J. Broas, N. G. Alexopolous, and E. Yablonovitch, "High-impedance electromagnetic surfaces with a forbidden frequency band," *IEEE Trans. Microw. Theory Tech.*, vol. 47, no. 11, pp. 2059–2074, Nov. 1999.

[14] A. Vallecchi, J. R. De Luis, F. Capolino, and F. De Flaviis, "Low profile fully planar folded dipole antenna on a high impedance surface," *IEEE Trans. Antennas Propag.*, vol. 60, no. 1, pp. 51–62, Jan. 2012.

[15] G. Donzelli, A. Vallecchi, F. Capolino, and A. Schuchinsky, "Metamaterial made of paired planar conductors: Particle resonances, phenomena and properties," *Metamaterials*, vol. 3, pp. 10–27, Mar. 2009.

[16] D. Tianwei, C. Zhiming, and Y. P. Zhang, "Coupling mechanisms and effects between on-chip antenna and inductor or coplanar waveguide," *IEEE Trans. Electron Devices*, vol. 60, no. 1, pp. 20–27, Jan. 2013.

[17] F. Yang and Y. Rahmat-Samii, "Reflection phase characterizations of the EBG ground plane for low profile wire antenna applications," *IEEE Trans. Antennas Propag.*, vol. 51, no. 10, pp. 2691–2703, Oct. 2003.

[18] H. Mosallaei and K. Sarabandi, "Antenna miniaturization and bandwidth enhancement using a reactive impedance substrate," *IEEE Trans. Antennas Propag.*, vol. 52, no. 9, pp. 2403–2414, Sep. 2004.

[19] S. R. Best and D. L. Hanna, "Design of a broadband dipole in close proximity to an EBG ground plane," *IEEE Antennas Propag. Mag.*, vol. 50, no. 6, pp. 52–64, Dec. 2008.

[20] A. Vallecchi, J. R. De Luis, F. Capolino, and F. De Flaviis, "Low profile fully planar folded dipole antenna on a high impedance surface," *IEEE Trans. Antennas Propag.*, vol. 60, no. 1, pp. 51–62, Jan. 2012.

[21] C. Guclu, J. Sloan, S. Pan, and F. Capolino, "Direct Use of the high impedance surface as an antenna without dipole on top," *IEEE Antennas Wireless Propag. Lett.*, vol. 10, pp. 1536–1539, 2011.

[22] P. Baccarelli, F. Capolino, S. Paulotto, and A. Yakovlev, "In-plane modal analysis of a metalayer formed by arrayed pairs of dogbone-shaped conductors," *Metamaterials*, vol. 5, pp. 26–35, 2011.
[23] A. A. Oliner and D. R. Jackson, "Leaky-wave antennas," in *Antenna Engineering Handbook*. New York, NY, USA: McGraw-Hill, 1993, vol. 4.
[24] F. Capolino, D. R. Jackson, and D. R. Wilton, "Fundamental properties of the field at the interface between air and a periodic artificial material excited by a line source," *IEEE Trans. Antennas Propag.*, vol. 53, no. 1, pp. 91–99, Jan. 2005.
[25] F. Capolino, D. R. Jackson, D. R. Wilton, and L. B. Felsen, "Comparison of methods for calculating the field excited by a dipole near a 2-D periodic material," *IEEE Trans. Antennas Propag.*, vol. 55, no. 6, pp. 1644–1655, Jun. 2007.
[26] F. Capolino, *Metamaterials Handbook*. Boca Raton, FL, USA: CRC, 2009.
[27] G. Lovat, P. Burghignoli, and D. R. Jackson, "Fundamental properties and optimization of broadside radiation from uniform leaky-wave antennas," *IEEE Trans. Antennas Propag.*, vol. 54, no. 5, pp. 1442–1452, May 2006.
[28] F. Capolino, A. Vallecchi, and M. Albani, "Equivalent transmission line model with a lumped X-circuit for a metalayer made of pairs of planar conductors," *IEEE Trans. Antennas Propag.*, vol. 61, no. 2, pp. 852–861, Feb. 2013.
[29] N. Marchand, "Transmission-line conversion transformers," *Electronics*, vol. 17, no. 12, pp. 142–145, Dec. 1944.
[30] A. K. Sen and I. D. Robertson, "Analysis and design of impedance-transforming planar Marchand baluns," *IEEE Trans. Microw. Theory Tech.*, vol. 49, no. 2, pp. 402–406, Feb. 2001.
[31] W. Zheng, C. Pei-Yuan, P. Nazari, W. Chun-Cheng, C. Zhiming, and P. Heydari, "A 210 GHz fully integrated differential transceiver with fundamental-frequency VCO in 32 nm SOI CMOS," in *IEEE Int. Solid-State Circuits Conf. Dig. Tech. Papers (ISSCC)*, 2013, pp. 136–137.
[32] J. X. Liu, C. Y. Hsu, H. R. Chuang, and C. Y. Chen, "A 60-GHz millimeter-wave CMOS Marchand balun," in *Proc. IEEE Radio Frequency Integrated Circuits (RFIC) Symp.*, 2007, pp. 445–448.
[33] C. Meng-Ju, W. Hsien-Shun, and C. K. C. Tzuang, "A compact CMOS Marchand balun incorporating meandered multilayer edge-coupled transmission lines," in *IEEE MTT-S Int. Microwave Symp. Dig. (MTT '09)*, 2009, pp. 125–128.
[34] W. M. Fathelbab and M. B. Steer, "New classes of miniaturized planar Marchand baluns," *IEEE Trans. Microw. Theory Tech.*, vol. 53, no. 4, pp. 1211–1220, Apr. 2005.
[35] S. Beer and T. Zwick, "Probe based radiation pattern measurements for highly integrated millimeter-wave antennas," in *Proc. 4th Eur. Conf. Antennas Propag. (EuCAP)*, 2010, pp. 1–5.
[36] S. A. Hosseini, F. Capolino, and F. De Flaviis, "A 44 GHz single-Feed Fabry-Parot Cavity antenna designed and fabricated on quartz," in *Proc. IEEE Int. Symp. Antennas Propag. (APSURSI)*, 2011, pp. 1285–1288.
[37] A. Babakhani, X. Guan, A. Komijani, A. Natarajan, and A. Hajimiri, "A 77-GHz phased-array transceiver with on-chip antennas in silicon: Receiver and antennas," *IEEE J. Solid-State Circuits*, vol. 41, pp. 2795–2806, Dec. 2006.
[38] M. R. Nezhad-Ahmadi, M. Fakharzadeh, B. Biglarbegian, and S. Safavi-Naeini, "High-efficiency on-chip dielectric resonator antenna for mm-wave transceivers," *IEEE Trans. Antennas Propag.*, vol. 58, no. 10, pp. 3388–3392, Oct. 2010.
[39] H. Debin, X. Yong-Zhong, G. Wang-Ling, H. Sanming, H. Wei, and M. Madihian, "130-GHz on-chip meander slot antennas with stacked dielectric resonators in standard CMOS technology," *IEEE Trans. Antennas Propag.*, vol. 60, no. 9, pp. 4102–4109, Sep. 2012.
[40] N. Behdad, D. Shi, H. Wonbin, K. Sarabandi, and M. P. Flynn, "A 0.3 $\mathrm{mm}^2$ miniaturized X-band on-chip slot antenna in 0.13 mu m CMOS," in *Proc. IEEE Radio Freq. Integr. Circuits (RFIC) Symp.*, Honolulu, HI, USA, 2007, pp. 441–444.
[41] H. Kuo-Ken and D. D. Wentzloff, "60 GHz on-chip patch antenna integrated in a 0.13-$\mu$m CMOS technology," in *Proc. IEEE Int. Conf. Ultra-Wideband (ICUWB)*, 2010, pp. 1–4.
[42] M. Uzunkol, O. D. Gurbuz, F. Golcuk, and G. M. Rebeiz, "A 0.32 THz SiGe $4 \times 4$ imaging array using high-efficiency on-chip antennas," *IEEE J. Solid-State Circuits*, vol. 48, pp. 2056–2066, 2013.
[43] H. Ben Elhaj Moussa, F. Torres, G. Z. El Nashef, B. Barelaud, and E. Ngoya, "Integrated on-chip antenna on silicon for millimeter-wave applications," in *Proc. 13th Mediterranean Microw. Symp. (MMS)*, 2013, pp. 1–4.
[44] H. Sanming, X. Yong-Zhong, Z. Bo, W. Lei, L. Teck-Guan, J. Minkyu, and M. Madihian, "A SiGe BiCMOS transmitter/receiver chipset with on-chip SIW antennas for terahertz applications," *IEEE J. Solid-State Circuits*, vol. 47, no. 11, pp. 2654–2664, Nov. 2012.
[45] S. Eunyoung, S. Dongha, M. Chuying, H. Ruonan, S. Sankaran, C. Changhua, W. Knap, and K. O. Kenneth, "Progress and challenges towards terahertz CMOS integrated circuits," *IEEE J. Solid-State Circuits*, vol. 45, no. 8, pp. 1554–1564, Aug. 2010.
[46] Q. J. Gu, Z. Xu, J. Heng-Yu, P. Bo, X. Xiaojing, M. C. F. Chang, L. Wei, and H. Fetterman, "CMOS THz generator with frequency selective negative resistance tank," *IEEE Trans. Terahertz Science Technol.*, vol. 2, no. 2, pp. 193–202, Mar. 2012.
[47] T. Hirano, K. Okada, J. Hirokawa, and M. Ando, "60 GHz on-chip patch antenna integrated in a 0.18-$\mu$m CMOS technology," in *Proc. Int. Symp. Antennas Propag. (ISAP)*, 2012, pp. 62–65.

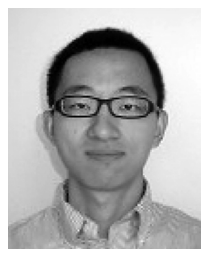

**Shiji Pan** (S'10), received the B.S. degree in electrical engineering from the Shanghai Jiao Tong University, Shanghai, China, in 2007, the M.S. degree in electrical engineering from the University of Houston, Houston, TX, USA, in 2009, and the Ph.D. degree in electrical engineering from the University of California, Irvine, CA, USA, in 2014.

He is currently with Broadcom Cooperation, Irvine, CA, where he is a Senior Staff Scientist, working on signal and power integrity. He has published more than 20 peer-reviewed journal articles and conference papers and coauthored one book chapter. His research interests include millimeter wave antennas, analog circuits, signal integrity, and power integrity.

**Francis Caster II** (M'87) received the B.S.E.E. degree from California State University, Fullerton, USA, in 1984 and the M.S. degree in electrical engineering from the University of California Irvine (UCI), Irvine, CA, USA, in 2012. He is currently pursuing a Ph.D. degree in electrical engineering at UC Irvine.

His present research in the Nanoscale Communications Integrated Circuits Lab at UCI focuses on silicon-based millimeter-wave and sub-millimeter-wave circuits and systems-on-chip at frequencies from 5 GHz up to 500 GHz. His research here led to the biggest RF chip designed to date by the lab, a 6 mm × 6 mm W-band 9-element imaging array receiver, the subject of this paper. Prior to his graduate studies he was an analog/mixed-signal Design Engineer at Rockwell International from 1979 to 1990, and also briefly held positions at VTC and Globespan in the late 1990s. In 1990, he started a consulting company providing design and layout services for CMOS/BiCMOS circuits and systems primarily covering baseband mixed-signal ICs in analog front ends for disk drives and for DSL chipsets. He has since expanded to sub-THz frequencies. His present interests include CMOS/BiCMOS circuits and systems covering baseband through sub-THz frequencies. He holds two patents and is the coauthor of several papers.

**Payam Heydari** (S'98–M'00–SM'07) received the B.S. and M.S. degrees (with honors) in electrical engineering from the Sharif University of Technology, Tehran, Iran, in 1992 and 1995, respectively. He received the Ph.D. degree in electrical engineering from the University of Southern California, Los Angeles, CA, USA, in 2001.

In August 2001, he joined the University of California, Irvine, where he is currently a Professor of Electrical Engineering. His research covers the design of terahertz/millimeter-wave/RF and analog in-

tegrated circuits. He is the (co)-author of two books, one book chapter, and more than 110 journal and conference papers.

Dr. Heydari was a Guest Editor of IEEE JOURNAL OF SOLID-STATE CIRCUITS. He was an Associate Editor of the IEEE TRANSACTIONS ON CIRCUITS AND SYSTEMS – part I from 2006 to 2008. He was a Technical Program Committee member of the IEEE Compound Semiconductor IC Symposium, IEEE Custom Integrated Circuits Conference (CICC), and International Symposium on Low-Power Electronics and Design (ISLPED). He has given Keynote Speech to *IEEE GlobalSIP 2013 Symposium on Millimeter Wave Imaging and Communications* and served as Invited Distinguished Speaker to the *2014 IEEE Midwest Symp. Circuits and Systems*. He currently serves on the Technical Program Committee of the IEEE International Solid-State Circuits Conference (ISSCC). He is the Distinguished Lecturer of the IEEE Solid-State Circuits Society. The Office of Technology Alliances at UCI has named Dr. Heydari one of 10 outstanding innovators at the university. He is the corecipient of the 2009 Business Plan Competition First Place Prize Award and Best Concept Paper Award both from Paul Merage School of Business at UC-Irvine. He is the recipient of the 2010 Faculty of the Year Award from UC-Irvine's Engineering Student Council (ECS), the 2009 School of Engineering Best Faculty Research Award, the 2007 IEEE Circuits and Systems Society Guillemin-Cauer Award, the 2005 NSF CAREER Award, the 2005 IEEE Circuits and Systems Society Darlington Award, the 2005 UCI's School of Engineering Teaching Excellence Award, the Best Paper Award at the 2000 IEEE International Conference on Computer Design (ICCD), the 2000 Honorable Award from the Department of EE-Systems at the University of Southern California, and the 2001 Technical Excellence Award in the area of Electrical Engineering from the Association of Professors and Scholars of Iranian Heritage (APSIH). He was recognized as the 2004 Outstanding Faculty at the UCI's EECS Department. His research on novel low-power multi-purpose multi-antenna RF front-ends received the Low-Power Design Contest Award at the 2008 *IEEE Int'l Symposium on Low-Power Electronics and Design (ISLPED)*.

**Filippo Capolino** (S'94–M'97–SM'04) received the Laurea (*cum laude*) and the Ph.D. degrees in electrical engineering from the University of Florence, Florence, Italy, in 1993 and 1997, respectively.

He is currently an Associate Professor at the Department of Electrical Engineering and Computer Science of the University of California, Irvine, CA, USA. Previously he has been an Assistant Professor at the Department of Information Engineering of the University of Siena, Siena. Italy. From 1997 to 1999, he was a Fulbright Researcher and Postdoctoral Fellow with the Department of Aerospace and Mechanical Engineering, Boston University, Boston, MA, USA. From 2000 to 2001, part of 2005 and in 2006, he was a Research Assistant Visiting Professor with the Department of Electrical and Computer Engineering, University of Houston, Houston, TX, USA. He has been a short-term Visiting Professor at the Fresnel Institute, Marseille, France (2003) and at the Centre de Recherche Paul Pascal, Bordeaux, France (2010). His research interests include millimeter-wave antennas, metamaterials and their applications, traveling-wave tubes, sensors in both microwave and optical ranges, wireless systems, chip-integrated antennas and applied electromagnetics in general. He was a founder and the EU Coordinator of the EU Doctoral Programs on Metamaterials from 2004 to 2009.

Dr. Capolino is also a member of OSA and SPIE. He received the R. W. P. King Prize Paper Award from the IEEE Antennas and Propagation Society for the Best Paper of the Year 2000, by an author under 36. In 2014 he received the Best Antenna Theory Paper Award, at the European Conference on Antennas and Propagation (EUCAP), The Hague, Netherlands.

From 2002 to 2008, he served as an Associate Editor for the IEEE TRANSACTIONS ON ANTENNAS AND PROPAGATION. He is the Editor of the *Metamaterials Handbook* (CRC, 2009).